This article has been accepted for inclusion in a future issue of this journal. Content is final as presented, with the exception of pagination.

Galvanic-Coupled Trans-Dural Data Transfer for High-Bandwidth Intracortical Neural Sensing

Chengyao Shi, *Student Member, IEEE*, Minyoung Song, *Member, IEEE*, Zhenyu Gao, Andrea Bevilacqua, *Senior Member, IEEE*, Guido Dolmans, and Yao-Hong Liu, *Senior Member, IEEE*

***Abstract*— A digital-impulse galvanic coupling as a new high-speed trans-dural (from cortex to the skull) data transmission method has been presented in this article. The proposed wireless telemetry replaces the tethered wires connected in between implants on the cortex and above the skull, allowing the brain implant to be "free-floating" for minimizing brain tissue damage. Such trans-dural wireless telemetry must have a wide channel bandwidth for high-speed data transfer and a small form factor for minimum invasiveness. To investigate the propagation property of the channel, a finite-element model is developed, and a channel characterization based on a liquid phantom and porcine tissue is performed. The results show that the trans-dural channel has a wide frequency response of up to 250 MHz. Propagation loss due to micromotion and misalignments is also investigated in this work. The result indicates that the proposed transmission method is relatively insensitive to misalignment. It has approximately 1-dB extra loss when there is a horizontal misalignment of 1 mm. A pulse-based transmitter application-specific integrated circuit (ASIC) and a miniature printed circuit board (PCB) module are designed and validated *ex vivo* with a 10-mm-thick porcine tissue. This work demonstrates a high-speed and miniature in-body galvanic-coupled pulse-based communication with a data rate up to 250 Mb/s with an energy efficiency of 2 pJ/bit and has a small module area of only 26 mm^2.**

***Index Terms*— Body channel communication (BCC), brain–computer interfaces, galvanic coupling (GC), implantable transceivers, neural interface, trans-cranial, trans-dural, wireless telemetry.**

I. Introduction

WITH the strong demand for helping patients suffering from neural disorders (e.g., Parkinson and stroke) to regain their sensory-motor or cognitive functions, the need for neural interfaces is becoming acute in the coming decades. Intracortical microelectrode arrays (MEAs) continue to remain the gold standard for neural interfaces and enable electrical sensing with submillisecond temporal resolution and tens of micrometer spatial resolution, making this the most widely adopted clinical method at the moment. With the recent introduction of high-density MEAs (e.g., silicon probe [1], [2] or polymer probe [3] with up to 1000 electrodes), neuroscientists can increase the density of neural sensing [4]. Assuming each recording channel is sampled with a 10-bit ADC at 25 ksamples/s, the total amount of data that need to be transferred can reach 250 Mb/s. Although data compression techniques can relax the bandwidth required for data transmission, the capability of providing raw data from an implantable device is still highly preferred for diagnosis and optimization reasons. Currently, most of the implantable neural sensors reported in the literature, for recording intracortical extracellular single-unit neural activities from the brain, do not apply data compression before wireless transmission [5], [6]. High fidelity data are crucial for neuroscience research, and potential distortion due to compression is avoided.

MEAs are typically implanted via craniotomy, which requires surgery on a large skull surface area, resulting in a long period of convalescence. With the recent advancement in craniotomy, a new burr-hole craniotomy can safely open a small hole [7], with a diameter less than 10 mm, and allows the skull to also heal much more quickly than conventional large-area craniotomies. However, the existing telemetry modules are still too large to be fully implanted below the skull. Having a direct cable connection between the telemetry module and the MEA, the latter is bounded in its movements and is not completely free to follow the motion of the brain. Therefore, it will also have relative movements with respect to the brain, causing damage to the surrounding brain tissue. This leads to serious scarring and affects the quality of the recording [8]. Hence, a miniature and wideband wireless link that transmits sensor data across the dura (a brain protection tissue) and scalp is a critical part to make the MEA "free-floating," less invasive surgically, and offer a highly preferable option in clinics [8], [9], [10].

A few of the existing preclinical intracortical neural interface systems with one or multiple MEAs were validated on primates [4], [11], [12], including a large head-mounted telemetry module, as shown in Fig. 1(a). Patients with such modules suffer from huge risk due to physical accidents and infections. These head-mounted telemetry modules have been miniaturized and implanted below the scalp in [13] and [14], i.e., as a transcutaneous telemetry module,

Manuscript received 26 April 2022; revised 30 June 2022; accepted 17 July 2022. This work was supported by the European Research Council (ERC) through the European Union's Horizon 2020 Research and Innovation Program under Grant 101001448. *(Corresponding author: Chengyao Shi.)*

Chengyao Shi and Guido Dolmans are with the Department of Electrical Engineering, Eindhoven University of Technology (TU/e), 5612 AZ Eindhoven, The Netherlands (e-mail: c.shi@tue.nl; g.dolmans@tue.nl).

Minyoung Song and Yao-Hong Liu are with imec, 5656 AE Eindhoven, The Netherlands (e-mail: minyoung.song@imec.nl).

Zhenyu Gao is with the Department of Neuroscience, Erasmus MC, 3015 GD Rotterdam, The Netherlands (e-mail: z.gao@erasmusmc.nl).

Andrea Bevilacqua is with the Department of Information Engineering, University of Padua, 35131 Padua, Italy (e-mail: andrea.bevilacqua@dei.unipd.it).

Color versions of one or more figures in this article are available at https://doi.org/10.1109/TMTT.2022.3198100.

Digital Object Identifier 10.1109/TMTT.2022.3198100

0018-9480 © 2022 IEEE. Personal use is permitted, but republication/redistribution requires IEEE permission.
See https://www.ieee.org/publications/rights/index.html for more information.

Authorized licensed use limited to: IMEC. Downloaded on September 15,2022 at 08:09:51 UTC from IEEE Xplore. Restrictions apply.

This article has been accepted for inclusion in a future issue of this journal. Content is final as presented, with the exception of pagination.

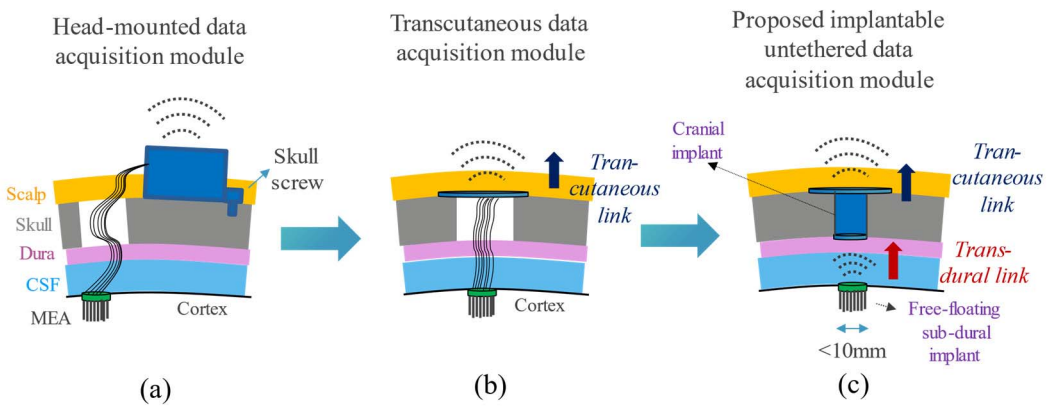

Fig. 1. State-of-the-art head-mounted data acquisition module and the proposed untethered data acquisition module with free-floating MEAs. (a) Tethered head-mounted telemetry module. (b) Tethered transcutaneous telemetry module. (c) Proposed implantable telemetry with a tether-less trans-dural link.

as shown in Fig. 1(b), avoiding risks mentioned above. However, one remaining critical issue is the strain and micromotions resulting from the MEA being tethered by bundles of cumbersome wires to either the head-mounted or the transcutaneous telemetry module, as shown in Fig. 1(a) and (b), which leads to severe scarring [8]. Furthermore, the neural decoding of iBCIs requires frequent (daily basis) calibrations to accommodate the signal drift due to MEA moved by the tethering wire [15].

As illustrated in Fig. 1(c), the neural sensing data from MEAs will be transmitted across the channel containing cerebrospinal fluid (CSF) and dura and be received by a cranial implant (or "cranial plug") that resides in the skull-hole volume (with a diameter smaller than 10 mm), i.e., a "trans-dural" link. The cranial implant with less volume constraints than the subdural implant then "relays" the data transcutaneously to the external device [13].

To the best of the author's knowledge, there is no wireless transmission method reported in the literature that can support such trans-dural link, coupling high-speed data (>250 Mb/s) efficiently across biological tissues, in this case, approximately 1–4 mm dura and 3–5 mm CSF, and fitting to a limited module area well below 100 mm^2.

The solutions presented in the literature based on far-field electromagnetic (EM) radiation [16], [17], [18] suffer from the bandwidth-area tradeoff of antennas [19]. The dimension of the antenna must be comparable to the half wavelength of the transmitted signals to achieve optimum radiation efficiency. A high-frequency signal with a shorter wavelength can reduce the antenna dimension, but it suffers from the shadowing effect caused by the body, which increases the attenuation [20]. Alternatively, an electrically small antenna (i.e., antenna dimension $< \lambda/10$) has a smaller area but has limited bandwidth and degraded radiation efficiency [21].

Inductive coupling [22], [23], [24] is widely adopted in implantable devices for wireless power and data transfer, but it also does not offer sufficient bandwidth due to a high quality-factor resonance required for efficient magnetic induction [25]. A large cross section is also needed to have low path loss and to minimize the impact of misalignment. The relation between the path loss and the quality factor is listed in the following equation, assuming that the transmitter and the receiver have coils with the same quality factor $Q_{\mathrm{Tx}} = Q_{\mathrm{Rx}} = Q$:

$$\mathrm{Path_gain} \approx k Q^2 \tag{1}$$

where k is the coupling coefficient between coils [26]. Wideband communication requires coils with low quality factor Q (= frequency/bandwidth), but this reduces path gain. Note the coil diameter and the coupling coefficient k are linked by the following equation:

$$k = \frac{1}{\left[1 + 2^{2/3}\left(\frac{d}{\sqrt{r_{\mathrm{Tx}} r_{\mathrm{Rx}}}}\right)^2\right]^{3/2}} \tag{2}$$

where d is the distance between the two coils, and r_{Tx} and r_{Rx} are the transmitter and the receiver coil radii, respectively [27]. Equations (1) and (2) indicate that there is a fundamental tradeoff between the coil size, path loss, and transmission bandwidth in inductive coupling.

Optical communication has been demonstrated to have sufficient bandwidth for data transmission up to hundreds of megabits per second, while potentially having a small footprint with miniature components such as vertical cavity surface emitting laser (VCSEL) [28]. However, the mesoscopic structure of CSF and dura is too scattered for optical communication, so the propagation distance is limited. In addition, it is reported that the link quality of the optical communication has poor immunity to the horizontal misalignment (<0.2 mm) [28].

Body channel communication (BCC) relies on the dielectric properties of the tissue to transmit electrical signals using the body as the communication medium, and galvanic coupling (GC) uses two electrodes, as the dipole coupler, to couple a differential signal to the tissue. The communication channel is typically operated in the reactive near field, i.e., the propagation distance is much shorter than the length of the dipole coupler and the signal wavelength. In such an operation region, a dipole is not radiative and its electrical field strength decays cubically with the distance ($1/d^3$). In this case, the dipole becomes more like a coupler, and its length is no

Authorized licensed use limited to: IMEC. Downloaded on September 15,2022 at 08:09:51 UTC from IEEE Xplore. Restrictions apply.

This article has been accepted for inclusion in a future issue of this journal. Content is final as presented, with the exception of pagination.

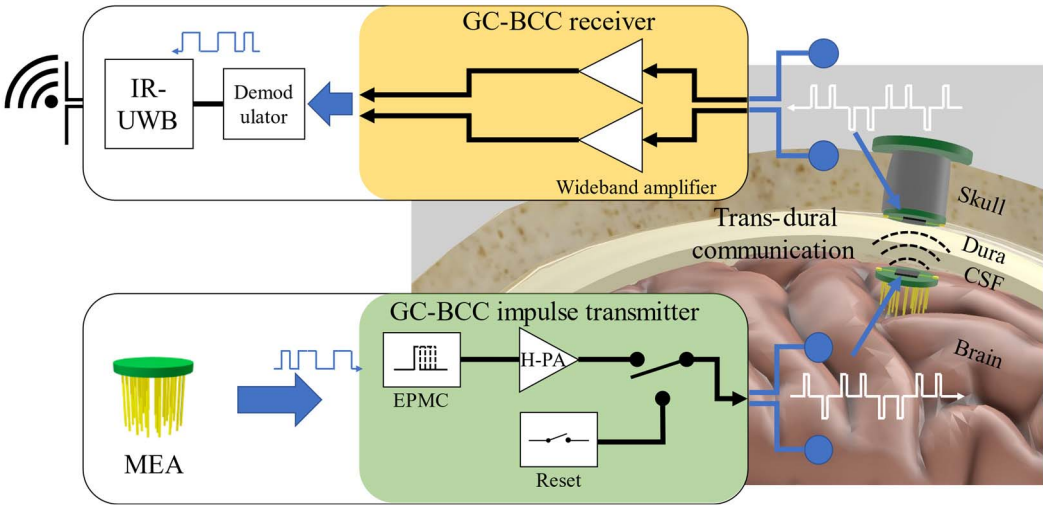

Fig. 2. Concept of the proposed trans-dural digital-impulse galvanic-coupled BCC link. The transmitter is positioned under the dura and near the MEA, and it receives the acquired data acquired by the probe. The data are modulated and sent through the GC-BCC to minimize power consumption. This minimizes the power consumption and increases the operation time of the deep-implanted device. The receiver, positioned under the skull, acquires the signal and transmits the data to an external unit through the UWB, which can then be positioned at a greater distance.

longer constrained by the wavelength of the signal. The dipole coupler of the transmitter generates a primary current flow between two electrodes of the coupler and a secondary current flow further away from the coupler. The secondary current flow induces a voltage difference between two electrodes of the dipole coupler of the receiver.

Galvanic-coupled BCCs (GC-BCCs) reported in the literature focus primarily on-body to on-body [29], [30], [31], [32] or on-body to implant [33], [34] communication using skin-attached electrodes with relatively large dimensions, which does not well represent the channel properties of implant-to-implant trans-dural communication in this work. Although GC has been employed for implant-to-implant intracardiac communication [35], [36], it only demonstrates an operation frequency up to 10 MHz for the ECG application. It is unclear whether such an implant-to-implant channel has sufficient bandwidth to transfer data up to hundreds of megabits per second for the target application. In this work, we aim to explore the bandwidth boundary of galvanic-coupled BCCs. Furthermore, we also investigated the impact of misalignments caused by the micromotion of the brain relative to the skull [2]. Finally, we designed a miniature CMOS GC-BCC transmitter IC employing a proposed "digital-impulse" modulation and validated the trans-dural data link with a biological tissue with the similar dielectric property.

The overall system concept is illustrated in Fig. 2. The proposed digital-impulse galvanic-coupled BCC is designed with the goal of transferring the data collected by the MEA neural sensor across the CSF and dura tissue, with high data rate. By leveraging broadband nature of the trans-dural channel identified in this work, the neural data are encoded and modulated by an encoding and pulse modulation circuit (EPMC) to return-to-zero impulses with only nanoseconds pulsewidth. This not only greatly improves energy consumption but also minimizes the charge accumulation at the electrode–tissue interface [37]. The binary data are represented by the polarity of the impulse. Both the transmitter and the receiver employ a dipole coupler to generate and sense, respectively, a confined electrical field. The diameter of each circular-shaped electrode of the dipole coupler is designed to be 0.55–1 mm, and the interelectrode distance (center-to-center) is 5.5–10 mm, such that the length of the dipole coupler can be fit within the burr hole. The choice of electrode dimension and the interelectrode distance (i.e., the length of the dipole coupler) is a tradeoff between implant area, path gain, and the H-bridge power amplifier's (H-PA) power consumption. A shorter length of the dipole coupler has more current flowing in between two electrodes of the transmitter's dipole coupler, thus resulting in a lower path gain and higher H-PA power consumption.

The impulse is coupled to the trans-dural channel through the dipole coupler of the transmitter. The corresponding GC-BCC receiver is to be placed in the cranial implant, right above the subdural implant. Since the cranial implant has a relatively larger volume and surface area above the skull, its power consumption requirement can be relaxed, as long as it does not cause tissue heating. The received data can then be relayed and transmitted transcutaneously by, e.g., an impulse-radio ultrawideband (IR-UWB) we developed in [13].

To deliver power wirelessly from the cranial implant to the millimeter-scale subdural implant, the tradition inductive powering approach will be inefficient. Inductive powering can also potentially distort the signal from GC-BCC due to the electrical coupling between them. To avoid such interference, powering solutions based on a nonelectrical method can be adopted, such as optical [38] or ultrasound [39], [40]. Since optical and ultrasound waves have short wavelength, they have been demonstrated in millimeter-scale implants. This work focuses on the high-speed trans-dural data link, so the wireless powering systems are beyond the research scope.

This article is organized as follows. Section II describes the numerical analysis of the BCC through the development of a finite element model. To verify the simulated model,

Authorized licensed use limited to: IMEC. Downloaded on September 15,2022 at 08:09:51 UTC from IEEE Xplore. Restrictions apply.

This article has been accepted for inclusion in a future issue of this journal. Content is final as presented, with the exception of pagination.

Section III describes the setup and the result of the *in vitro* channel characterization. In Section IV, we analyze the effect of the misalignment on the BCC. In Section V, the design of a CMOS transmitter IC is discussed in detail, and it is measured in an *ex vivo* setup to validate the trans-dural data communication. Finally, the discussion and conclusions are provided in Sections VI and VII, respectively.

II. Finite-Element Modeling

To study the propagation properties of the trans-dural channel, a simplified human-head model composed of human–brain tissues, i.e., gray matter, CSF, dura, and skull, is developed in COMSOL[1] Multiphysics simulator, as illustrated in Fig. 3(a). The model of a transmitter is positioned on top of the gray matter (i.e., the surface of the cortex), while the model of a receiver is positioned below the skull. The resulting transmission channel is therefore composed of a CSF layer and a dura layer. The frequency-dependent dielectric properties of each tissue composing the human-head model are based on the clinically validated Cole–Cole model reported in [41] and [42], and the thickness of each tissue layer is listed in Fig. 3(a), according to [43]. Note that the thickness of CSF and dura has a large variation between 4 and 9 mm, depending on the location of the cortex, gender, and age of the subjects.

A. Finite-Element Model

The simplified 3-D model of the human head is developed in COMSOL Multiphysics software using the ac/dc electric current module. The simulation assumes the quasi-static approximation to compute Maxwell's equation given the geometry of the model. This assumption is valid when the ratio between the channel length ($L = 10$ mm) and wavelength (λ) is lower than 1/10 [17], [44]. For the model in analysis, a signal at the frequency of 300 MHz has a wavelength in the tissue of about 100 mm, which therefore corresponds to the maximum frequency. Two electrodes of the dipole coupler are modeled as two metal disks, which are then excited with a sinusoidal voltage signal of 1-V (peak-to-peak) amplitude.

We also assume that the data are dc balanced with proper encoding, e.g., Manchester coding, so the low-frequency response of the medium below 50 MHz is neglected in the investigation. The space surrounding the head model is set as the ground to consider its electrical insulation [31].

The electrical potential distribution given by the simulation is shown in Fig. 3(a). The simulation results indicate that the frequency response of the transmission channel has a rather flat value of about −34 dB up to ∼250 MHz frequency, as shown in Fig. 6. This matches well with the calculated propagation gain based on the theoretical electric field distribution of the electric dipole in [29], which is approximately −38 dB. In addition, further simulations were carried out to verify the variation of the frequency response according to the type of tissue that makes up the transmission channel. These simulations were carried out maintaining the same geometries of the model and assigning to the channel the dielectric property of

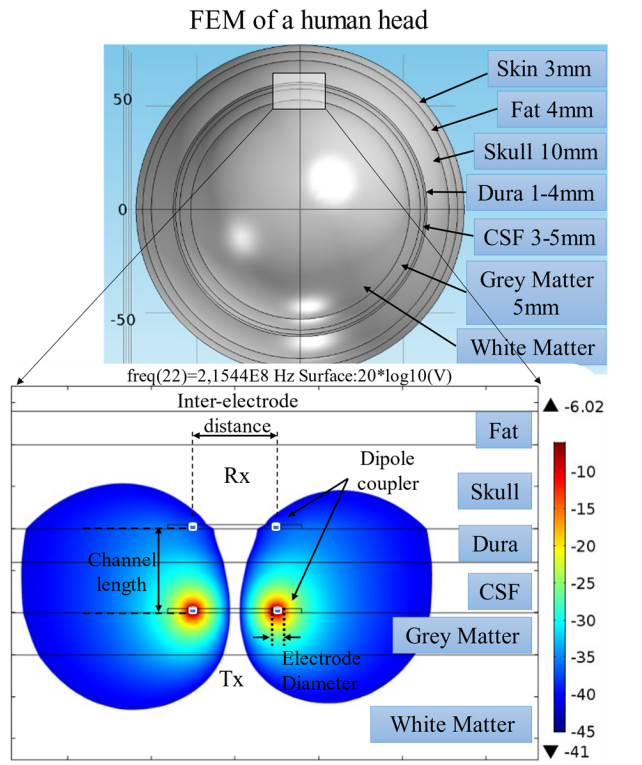

(a)

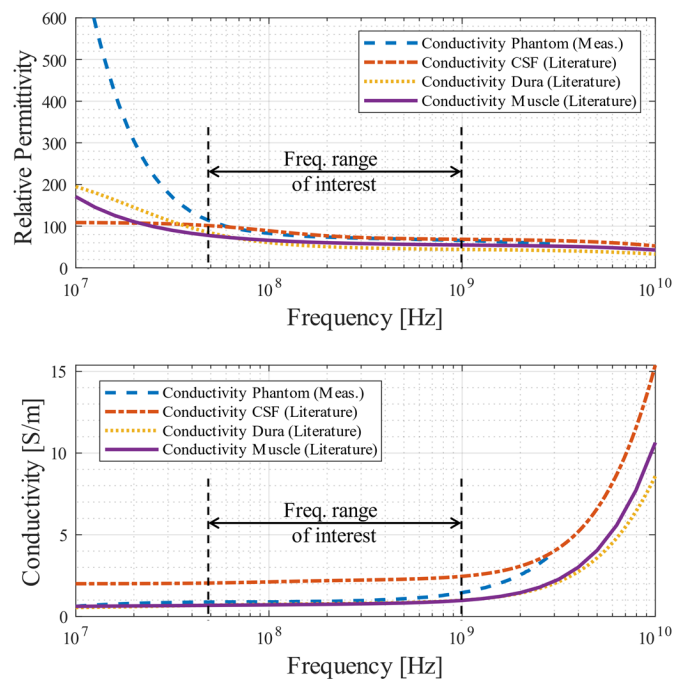

(b)

Fig. 3. FEM model representing a human head and magnification on an implanted transceiver that uses GC-BCC for communication. (a) Cross-sectional view of the electrical potential propagation through the trans-dural channel having a transmitter placed on the surface of the brain and a receiver placed above the dura. (b) Measured dielectric properties of the liquid phantom and dielectric properties of CSF, dura, and muscle tissue reported in [41] and [42]. The frequency band we are interested in is also indicated.

the biological tissue to be analyzed. The simulation results in Fig. 6 show that the path gain is relatively insensitive (<1 dB)

[1]Trademarked.

Authorized licensed use limited to: IMEC. Downloaded on September 15,2022 at 08:09:51 UTC from IEEE Xplore. Restrictions apply.

This article has been accepted for inclusion in a future issue of this journal. Content is final as presented, with the exception of pagination.

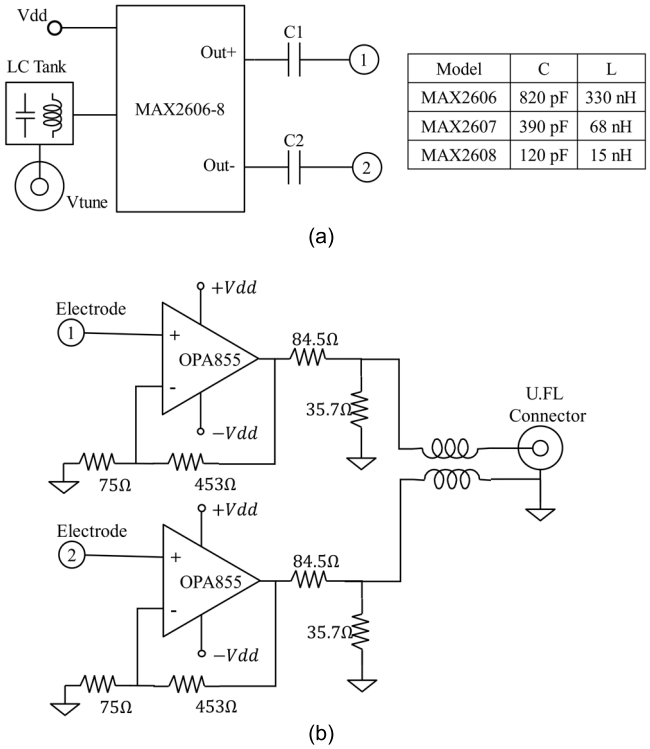

Model	C	L
MAX2606	820 pF	330 nH
MAX2607	390 pF	68 nH
MAX2608	120 pF	15 nH

Fig. 4. Schematic of the electronic module. (a) Schematic of the differential VCO. The output frequency of the VCO is controlled by the voltage at Vtune. The dc component is blocked by the series capacitors. The values for the inductance and the capacitance used are also indicated in the corresponding model of VCO. (b) Schematic of the receiver consists of two OPAMPs (OPA855) in a noninverting configuration. Both the VCO's and the receiver's electrodes have a diameter of 1 mm and an interelectrode distance of 10 mm.

to the dielectric property difference between tissues, e.g., CSF, dura, and muscle in the frequency band of interest (i.e., 50–1000 MHz). The simulated phase response versus frequency is also relatively constant with a small variation of ±0.1 rad.

III. In Vitro Channel Characterization

In order to verify the results obtained from the simulations, two custom boards were designed using discrete components. To model the transmission channel, a liquid phantom that has similar dielectric properties to a trans-dural channel was produced.

A. Electronic Module

The channel response is characterized with commercially available voltage-controlled oscillators (VCOs), MAX2606–2608 from maxim integrated as the signal source, as shown in Fig. 4(a). To cover a wide tuning range, each VCO covers a fraction of the frequency ranges, from 70 to 500 MHz, with an amplitude of 0.6 V (peak-to-peak). The input tuning voltage of each VCO, i.e., a dc control voltage (Vtune), is provided by a low-noise power supply Toellner TOE8733, which also provides the 3.3-V supply voltage. The inductance value for the VCO's resonator is selected according to the operating frequency. Capacitors $C1$ and $C2$ are required for dc blocking.

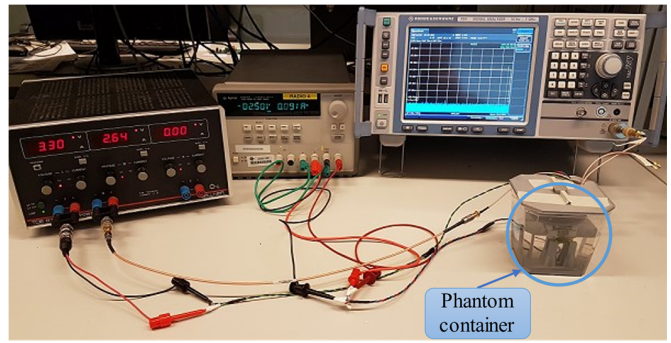

Fig. 5. *In vitro* characterization setup. The VCO and the receiver are hold in place by a 3-D printed structure contained inside a plastic box. The container is filled with the liquid phantom.

The receiver consists of two commercially available operational amplifiers (OPAMPs) in a noninverting configuration, as shown in Fig. 4(b). The OPAMPs are OPA855 from Texas Instruments, which are chosen for their 8-GHz gain–bandwidth product. They have a high input impedance of 5 kΩ and a low input capacitance of 0.2 pF. Note that a high input impedance and low input capacitance minimize the path loss due to loading effects. In this channel characterization, the electrodes of the dipole couplers have a diameter of 1 mm and an interelectrode distance of 10 mm, and the material of the electrodes is copper. Since the primary objective of this work is to demonstrate the feasibility of GC as a high-speed implant-to-implant communication method, the printed circuit board (PCB), except the dipole couplers, is insulated with epoxy to ensure it is watertight. It can be assumed that no wave propagation and reflection occurs between the dipole coupler and the transmitter or the receiver, so impedance matching is not required.

To calibrate the path gain of the whole measurement setup, a reference module is implemented, which directly connects the VCO output to the receiver input without dipole couplers. This reference setup serves the purpose of de-embedding the effects of the instruments, connection cables, and the electrical property of the VCO's and receiver's electronics.

B. Liquid Phantom and Testing Setup

A phantom that mimics the dielectric properties of the tissue is developed for the *in vitro* channel characterization. The liquid phantom is built by adjusting the salt and sugar ratio dissolved in the water according to [45]. The phantom was built to match as close as possible to the dielectric property of CSF and dura reported from the literature [41], [42] within the frequency range of interest. The measured dielectric properties (both permittivity and conductivity) of the phantom are shown in Fig. 3(b), which also includes data on CSF and dura reported in the literature.

The measurement was carried out with the spectrum analyzer P9375A in combination with the dielectric probe 85070E from Keysight Technologies. The liquid phantom also allows a flexible adjustment of the position of the VCO and receiver. The phantom is contained inside a transparent watertight container, and a 3-D printed structure holds the devices for stable testing, as shown in Fig. 5. The lower frame holds the

Authorized licensed use limited to: IMEC. Downloaded on September 15,2022 at 08:09:51 UTC from IEEE Xplore. Restrictions apply.

This article has been accepted for inclusion in a future issue of this journal. Content is final as presented, with the exception of pagination.

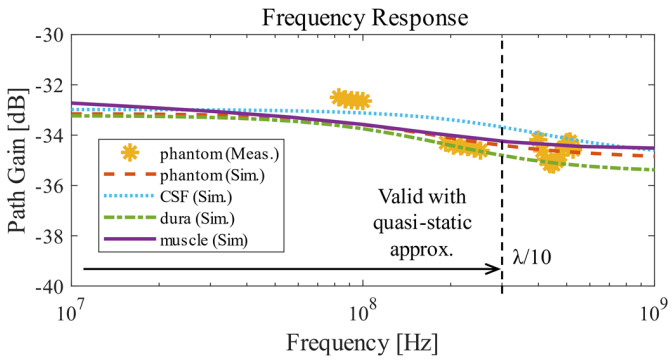

Fig. 6. Measured frequency response of GC BCC obtained from the *in vitro* measurement (yellow asterisk) and from the finite element simulation (solid lines) including phantom (red), CSF (blue), dura (green), and muscle (purple).

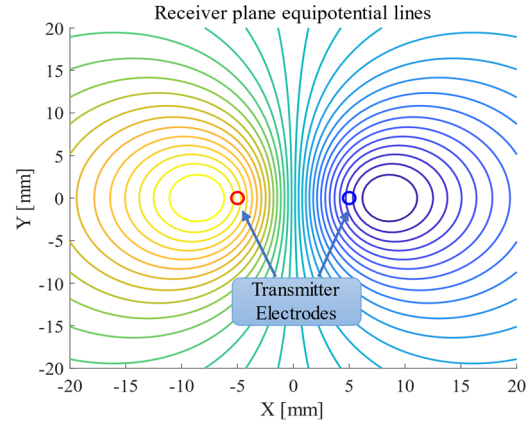

Fig. 7. Equipotential lines distribution at the receiver plane, i.e., 10 mm from the transmitter. The positions of the transmitter's dipole coupler are also indicated in this figure.

VCO PCB, while the top frame holds the receiver PCB and allows for easy rotation and horizontal movement.

Ground isolation and cable radiation are carefully considered when performing the channel characterization of the GC [29], [46]. Unwanted ground coupling can produce a ground loop between the VCO and receiver, and it can lead to the erroneous characterization of the path loss. For this reason, an isolation transformer, REOMED 1000, provides isolated supplies and grounds for the VCO and the receiver. Furthermore, long signal cables can introduce radiation, coupling from unwanted sources, as well as signal attenuation [46]. Similar to the approach presented in [32], [35], [46], and [47], we use differential signals at both transmitter output and also receiver input/output to minimize the impact on the case of ground coupling. The choice of implementing a VCO transmitter rather than using a signal generator is to avoid as much as possible such couplings between signal cables from the transmitter's input and the receiver's output. The connection wires of the transmitter input contain only dc signals for controlling the oscillation frequency of the VCO. Hence, it will not lead to wrong channel characterization even if the coupling between cables exists.

C. In Vitro Channel Frequency Response

The frequency response of the channel composed of the liquid phantom is illustrated in Fig. 6 (yellow points). It is then compared with the result obtained from the simulation by defining the dielectric properties of the channel with those measured with the phantom (red line). Furthermore, the results of the simulations for different biological tissues are shown for comparison in Fig. 6. Due to the limited frequency control range of the VCOs, only discrete points within the frequency range of interest are measured.

The results of *in vitro* channel characterization match well with the developed finite element model, with a difference below ±2 dB across the interested frequency range. The results also show a rather flat frequency response from 50- to 250-MHz frequency range. The path gain, defined as $G = V_{\mathrm{RX}}/V_{\mathrm{TX}}$, where V_{RX} is the signal voltage at the receiver and V_{TX} is the transmitted signal, is approximately −34 dB with a slightly lower value at the higher frequency.

IV. Influence of Misalignment

A galvanic-coupled BCC with a millimeter-scale dipole coupler can be influenced by misalignments, especially due to brain micromotion which can be up to ±4 mm [48]. In this work, we investigated the effect of the two types of misalignments: orientational and horizontal.

A. Horizontal Misalignment

Investigations for horizontal misalignment are performed in three directions: x, y, and $x + y$, as illustrated in Fig. 8(a).

Measurement of the path gain is taken for 5- and 10-mm horizontal shifts in three directions. The measurements were performed at the frequency of 200 MHz.

For either x- or y-directions, the path gain decrease is ∼1 dB/mm. For the horizontal misalignment in the $x + y$ direction (i.e., moving toward the direction of 45°), the result shows a lower path gain compared to the pure x or y shift. The path gain decreases up to 20.6 dB for a 10-mm misalignment (i.e., ∼2 dB/mm). The reason for this characteristic can be explained by the pattern of the equipotential line on the receiving plane, i.e., 10 mm above the plane of the transmitter's dipole coupler, as shown in Fig. 7. As gradually moving the receiver's dipole coupler in the x-direction, the potential of one electrode of the receiver dipole coupler increases initially and then decreases, while the potential of another electrode continuously decreases. For movements in the y-direction, the potential of both electrodes of the pair continuously decreases. Hence, the path loss is less sensitive to the x-direction [blue line in Fig. 8(a)] than to the y-direction [green line in Fig. 8(a)] for the length of the shifts approximately equal to the length of the coupler (i.e., 10 mm). Extra path loss due to the movement in the $x + y$-direction is approximately a superposition of the loss in both x- and y-directions.

B. Orientational Misalignment

An investigation for orientational misalignment is performed by setting the VCO at two frequencies, 100 and 200 MHz. A measurement of the path gain is taken every 10° of rotation

Authorized licensed use limited to: IMEC. Downloaded on September 15,2022 at 08:09:51 UTC from IEEE Xplore. Restrictions apply.

This article has been accepted for inclusion in a future issue of this journal. Content is final as presented, with the exception of pagination.

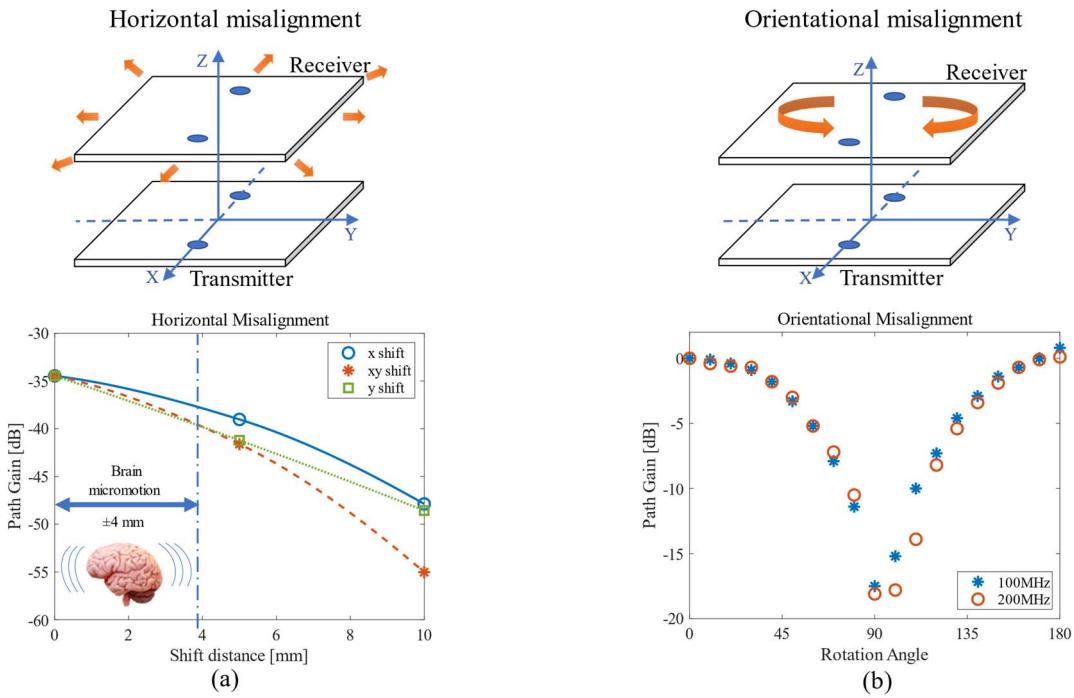

Fig. 8. Misalignment characterization. (a) Normalized path gain measurement results for horizontal misalignment in the x-, y-, and $x + y$-directions with shift of a 5 and 10 mm. (b) Normalized path gain measurement results for orientational misalignment for two different frequencies with progressive rotations of 10°.

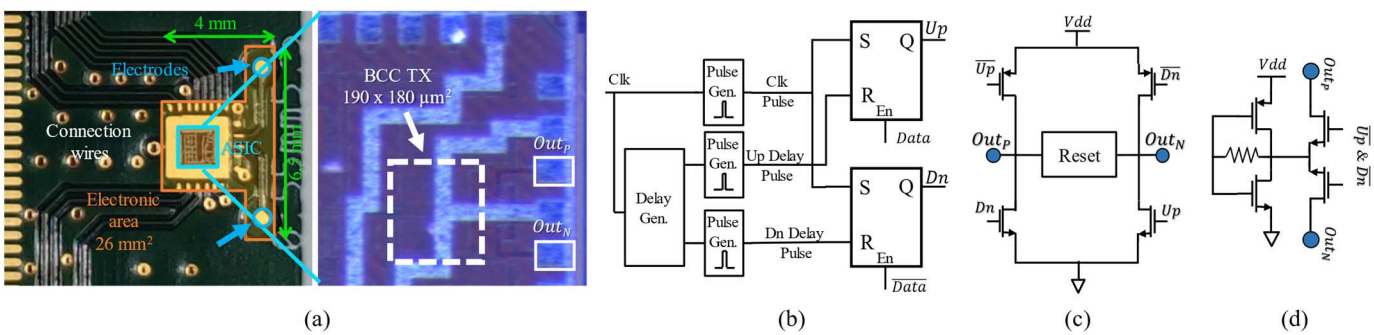

Fig. 9. GC-BCC digital-impulse transmitter ASIC and module. (a) PCB with the transmitter ASIC, and the zoomed-in view of the transmitter. The transmitter module area is 26 mm^2. (b) Schematic of the EPMC. (c) Schematic of the H-PA. (d) Reset circuit. At the reset signal, the two electrodes are connected together allowing the redistribution of the charge accumulated on the electrode–tissue interface.

between 0° and 180°. The results are shown in Fig. 8(b). For small rotation angle up to ±40°, the path gain degradation is limited to −3 dB. For larger angular rotation, the degradation in the path gain increases rapidly. For the worst case of 90° misalignment, the degradation is up to approximately 20 dB.

Note that brain micromotion typically does not include significant orientational movements. The static orientational misalignment is only introduced during the implantation, so it can be removed with one-time calibration, e.g., by visually aligning or by measuring the amplitude.

V. CMOS Digital-Impulse GC-BCC IC and Ex Vivo Validation

The possibility of using the GC-BCC as a method of transmitting impulsive signals has been validated with a CMOS application-specific integrated circuit (ASIC) with the biological tissue having similar dielectric properties as dura and CSF. This chip was fabricated in 28-nm CMOS technology and can generate pulses in the order of nanoseconds. The verification was carried out using porcine muscle tissue, which, as shown in Section III, has dielectric properties very similar to trans-dural tissues in the frequency range of interest.

A. High-Speed Digital Impulse Transmitter ASIC

A transmitter ASIC is designed to provide high-speed digital-impulse modulation and occupies a core silicon area of only 190 × 180 μm^2. The transmitter module area, including the ASIC and the dipole coupler, is within 4 × 6.5 mm^2, as shown in Fig. 9(a).

Authorized licensed use limited to: IMEC. Downloaded on September 15,2022 at 08:09:51 UTC from IEEE Xplore. Restrictions apply.

This article has been accepted for inclusion in a future issue of this journal. Content is final as presented, with the exception of pagination.

This ASIC composes of a 9-bit pseudorandom bit sequence generator (9 b-PRBS), an EPMC, an H-PA, and a reset circuit, as shown in Fig. 9(b)–(d). The 9-b-PRBS generates a pseudorandom bit stream to simulate the recorded neural sensor data at 250 Mb/ and 4-ns period. The data are encoded to a return-to-zero ternary data and modulated to biphasic impulses by a pulse modulation circuit. Positive and negative pulsewidths can be adjusted independently between 1 and 3 ns to test the frequency response and the impact of the charge imbalance [49]. The data are then driven from the dipole coupler to the tissue by the H-PA, as shown in Fig. 9(c). After each impulse, the reset circuit, shown in Fig. 9(d), discharges the residual charge accumulated at the electrode–tissue interface to maintain the charge balance.

Fig. 9(b) shows the EPMC. The clock signal and its delayed version control the "Set" and "Reset" input of the SR flip-flop, while the data signal controls the "Enable" input of the SR flip-flop. By adjusting the delay generator, the pulsewidth of the output signal can be adjusted. According to the input data, either the Up and $\overline{Up}$ switches are closed or the Dn and $\overline{Dn}$ switches are closed at the same time. After each pulse, the reset circuit connects the two electrodes and discharges the residual charge at the electrode–tissue interface. The output of the self-biased inverter in the reset circuit [Fig. 9(d)] defines the reset voltage, approximately half VDD. The reset time is primarily determined by the strength of the reset circuit and the tissue impedance. The double-layer capacitor from the electrode–tissue interface affects the reset time. A smaller dipole coupler and its electrodes have lower double-layer capacitance and thus a shorter reset time. The sizing of the reset switch also affects the achievable speed. Smaller reset switch has longer reset time, thus leading to longer symbol period. A timing control circuit is implemented in EPMC to ensure that the timing between Up, $\bar{\text{U}}$p, Dn, and $\bar{D}n$ signals does not overlap, avoiding a low impedance path between supply and ground.

B. Ex Vivo Validation With Biological Tissue

To further validate the actual signal propagation property with biological tissue under heterogeneous conditions, the BCC was performed with porcine muscle with a thickness of ∼10 mm, as illustrated in Fig. 10(a). As shown in Fig. 10(b), a motherboard connected to a field-programmable gate array (FPGA) and a notebook is used as an interface to control the ASIC and to provide the required clock. The connection between the motherboard and the ASIC is through a flexible cable. The data are generated by the on-chip PRBS to avoid possible coupling between connection cables due to the high-speed data link, while the configuration signal for the ASIC is provided by a notebook through a serial–peripheral interface (SPI) for one-time configuration. The receiver is connected to an oscilloscope Lecroy SDA816Zi with 40-Gs/s sampling speed. The transmitter ASIC is configured to send 1-ns return-to-zero pulse signal. During the idle state, i.e., when returning to 0, the reset circuit shorts two electrodes to allow charge redistribution and to remove the residual charge at the electrode–tissue interface [49]. The encapsulation was done with nonconductive epoxy glue, and the boards are fully coated except for the dipole coupler.

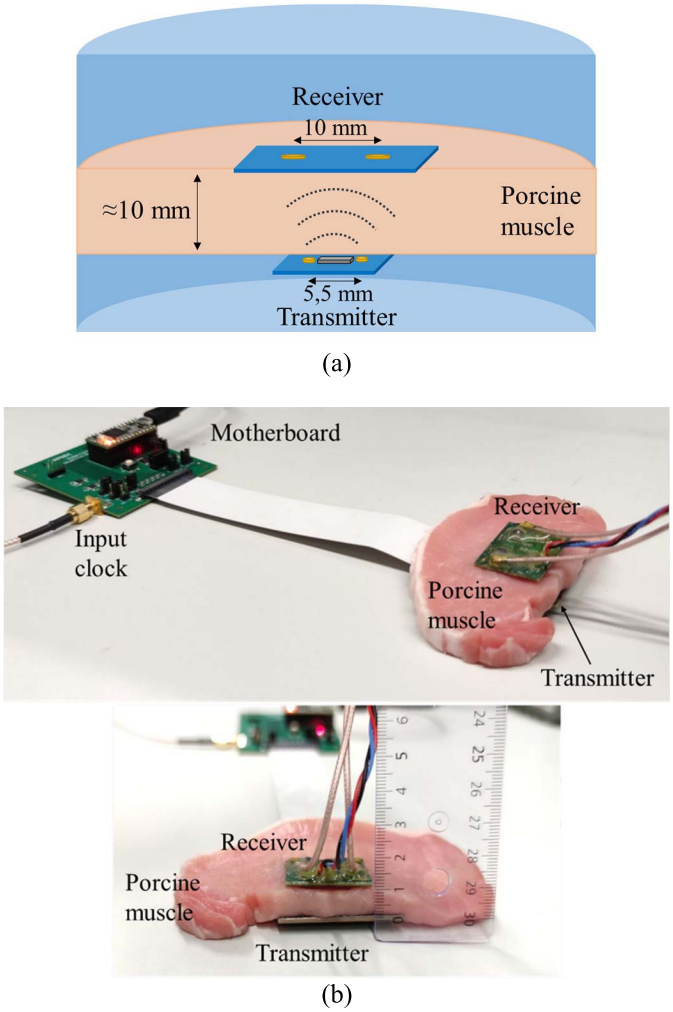

Fig. 10. *Ex vivo* validation setup. (a) Setup per *ex vivo* validation. (b) Measurement setup with the ASIC transmitter and porcine muscle.

Fig. 11(a) shows the partition of the average energy consumed by the ASIC. Approximately 25% of the energy is consumed by the EPMCs, while the remaining 75% is used by the H-PA and the reset circuit.

The measured eye diagram at the receiver output is shown in Fig. 11(b). The eye amplitude is approximately 6 mV, and the transmitter output voltage is ∼0.9 V, so the path gain is 43.5 dB. This matches well with the simulation based on the finite-element model presented in Section II-A. Compared to the channel characterization shown in Fig. 6, there is approximately 10-dB worse path loss. This is mainly because the length of dipole coupler used in the *ex vivo* validation is smaller than the one used in channel characterization (5.5 mm versus 10 mm). The eye diagram has an impulse and symbol period of 1 and 4 ns, respectively, with 0.8 ns of impulse settling time and 1.8 ns of reset time. A signal at the receiver output with ∼2 Mbit long was recorded. The bit-error rate (BER) of 2.4×10^{-6} was calculated by comparing the recorded data with the original transmitted PRBS data. To further lower the BER or to increase the communication

Authorized licensed use limited to: IMEC. Downloaded on September 15,2022 at 08:09:51 UTC from IEEE Xplore. Restrictions apply.

This article has been accepted for inclusion in a future issue of this journal. Content is final as presented, with the exception of pagination.

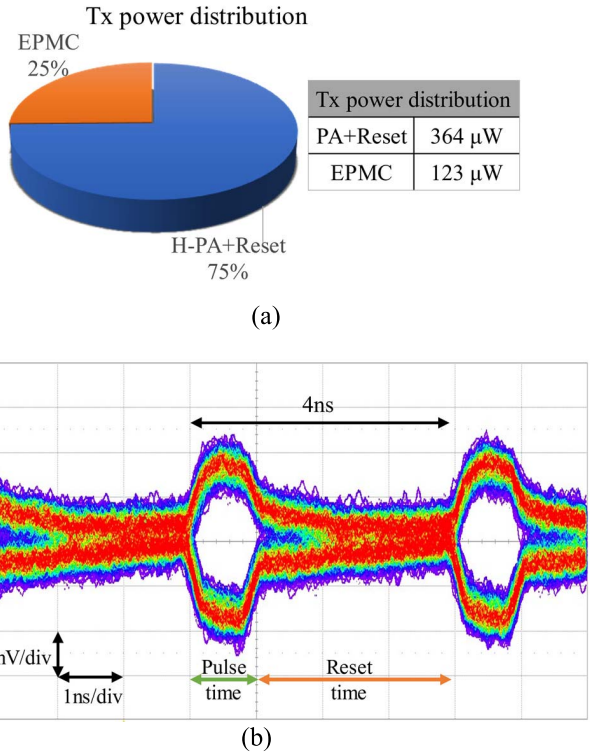

Fig. 11. Results of the *ex vivo* validation. (a) Transmitter ASIC power distribution chart. (b) Measured eye diagram of the received signal.

distance (i.e., the thickness of the tissue), the pulse time can be further increased to increase the energy per bit transmitted.

VI. Discussion

The *in vitro* characterization of the frequency response in liquid phantom shows a good agreement with the finite-element model, as shown in Fig. 6. It is observed that the amplitude response starts to "ring" from above ∼300 MHz, and the difference compared to the quasi-static finite-element model is gradually increased. This indicates that the dipole coupler starts entering the transition zone between near and far fields, i.e., midfield. The *ex vivo* validation with porcine muscle confirms that the wide frequency response of the channel can be exploited to directly transmit high-speed data up to 250 Mb/s. Signals with higher data rates can start becoming radiative, which has large amplitude fluctuation and is less efficient to couple.

Horizontal brain micromotion can reach up to ±4 mm when the head undergoes high accelerations, so the worst case path gain degradation for the proposed BCC due to horizontal movement is expected to be less than 5 dB, according to the characterization in Fig. 8(a). Even with the smaller dipole coupler used in *ex vivo* (with a length of 5.5 mm), the path degradation is expected to be less than 6 dB. In comparison to other in-body propagation methods, such as inductive coupling or optical, GC-BCC has better immunity to horizontal misalignment. Under similar coupler dimension and channel distance, optical transmission can only tolerate the horizontal misalignment below 1 mm [28], and the inductive coupling would also suffer from significant attenuation due to the degraded coupling coefficient.

TABLE I

Comparison With the State-of-the-Art High-Speed Implantable Transmitters

	This work	[23] TBIOCAS '19	[28] TBIOCAS '19	[13] ISSCC' 21
Propagation method	Digital-pulse GC-BCC	Inductive Coupling	Optical	IR-UWB
Data rate (Mbps)	**>250**	200	300	1660
Tx area (mm^2)	**26**	100 (coil area)	N.A. (discrete comp.)	105
Misalignment tolerance	**> 4 mm**	N.A.	0.2 mm	N.A.
Tissue thickness	10 mm (muscle)	11 mm (skull+skin)	4,25 mm (skin)	15 mm (skin)
Tx Power cons.	0.50 mW	0.30 mW	11 mW	9,69 mW
Tx Energy Efficiency	2 pJ/bit	1,5 pJ/bit	37 pJ/bit	5,8 pJ/bit

In Table I, the presented impulse-based galvanic-coupled BCC is benchmarked with the state-of-the-art high-speed (>200 Mb/s) and miniature implantable transmitters (Txs), including inductive coupling, optical and IR-UWB. The proposed GC-BCC demonstrates a data rate up to 250 Mb/s with a small electronic area of 26 mm^2, while most state-of-the-art GC-BCC communication [34], [35], [50] has limited bandwidth up to tens of megahertz. Inductive-coupled communication can achieve a higher data rate with a "de-Q" technique [23], but it suffers from high path loss and still requires a relatively large coil area. IR-UWB transmitters also require a large antenna to match the wavelength of the transmitted signals, which is difficult to reduce the area below 100 mm^2. Optical communication offers a high data rate but consumes high power and is sensitive to horizontal misalignment.

VII. Conclusion

We present an untethered trans-dural data transfer method based on digital-impulse galvanic-coupled BCC for high-bandwidth intracortical neural sensing. We have demonstrated that the bandwidth-volume-pathloss constraints in the conventional in-body far-field (e.g., EM radiation and optical) or near-field (e.g., inductive coupling) propagations can be overcome by using impulse-based GC.

A liquid phantom mimicking the biological tissue and galvanic-coupled devices was developed to characterize the channel response and the impact of misalignments. It shows that the galvanic-coupled BCC can tolerate the horizontal misalignment up to ±4 mm, which corresponds to the reported relative motion range of the brain.

A CMOS galvanic-coupled impulse-based transmitter ASIC is designed, and the transmitter module including the dipole coupler occupies a small area of 26 mm^2. The transmitter

Authorized licensed use limited to: IMEC. Downloaded on September 15,2022 at 08:09:51 UTC from IEEE Xplore. Restrictions apply.

This article has been accepted for inclusion in a future issue of this journal. Content is final as presented, with the exception of pagination.

device is validated *ex vivo* with the 10-mm-thick porcine muscle tissue. The work demonstrates a high-speed and miniature in-body galvanic-coupled communication, with a data rate up to 250 Mb/s and an energy efficiency of 2 pJ/bit. In comparison to other in-body communication methods, e.g., inductive, ultrasound, EM radiation, or optical, the proposed digital-impulse GC-BCC offers several benefits simultaneously, including high data rate, low power consumption, miniature form factor, and misalignment tolerance, which serves as the perfect candidate for trans-dural data transfer of high-channel-count and free-floating intracortical neural sensors.

Acknowledgment

The authors would like to thank Dr. R. Yadav for his guidance in modeling and Dr. A. M. Samoudi for his advice on phantom manufacturing.

References

[1] J. J. Jun *et al.*, "Fully integrated silicon probes for high-density recording of neural activity," *Nature*, vol. 551, no. 7679, pp. 232–236, Nov. 2017.

[2] N. A. Steinmetz *et al.*, "Neuropixels 2.0: A miniaturized high-density probe for stable, long-term brain recordings," *Science*, vol. 372, no. 6539, Apr. 2021.

[3] D.-Y. Yoon, S. Pinto, S. Chung, P. Merolla, T.-W. Koh, and D. Seo, "A 1024-channel simultaneous recording neural SoC with stimulation and real-time spike detection," in *Proc. Symp. VLSI Circuits*, Jun. 2021, pp. 1–2.

[4] D. A. Schwarz *et al.*, "Chronic, wireless recordings of large-scale brain activity in freely moving rhesus monkeys," *Nature Methods*, vol. 11, no. 6, pp. 670–676, Jun. 2014.

[5] M. Yin, D. A. Borton, J. Aceros, W. R. Patterson, and A. V. Nurmikko, "A 100-channel hermetically sealed implantable device for chronic wireless neurosensing applications," *IEEE Trans. Biomed. Circuits Syst.*, vol. 7, no. 2, pp. 115–128, Apr. 2013.

[6] J. Lee *et al.*, "Neural recording and stimulation using wireless networks of microimplants," *Nature Electron.*, vol. 4, no. 8, pp. 604–614, Aug. 2021.

[7] J.-T. Schantz *et al.*, "Cranioplasty after trephination using a novel biodegradable burr hole cover: Technical case report," *Operative Neurosurgery*, vol. 58, p. E176, Feb. 2006.

[8] L. Karumbaiah *et al.*, "Relationship between intracortical electrode design and chronic recording function," *Biomaterials*, vol. 34, no. 33, pp. 8061–8074, Nov. 2013.

[9] M. M. Ghanbari *et al.*, "A sub-mm^3 ultrasonic free-floating implant for multi-mote neural recording," *IEEE J. Solid-State Circuits*, vol. 54, no. 11, pp. 3017–3030, Nov. 2019.

[10] P. Yeon *et al.*, "Microfabrication, coil characterization, and hermetic packaging of millimeter-sized free-floating neural probes," *IEEE Sensors J.*, vol. 21, no. 12, pp. 13837–13848, Jun. 2021.

[11] M. Yin *et al.*, "Wireless neurosensor for full-spectrum electrophysiology recording during free behavior," Neuron, vol. 84, no. 6, pp. 1170–1182, Dec. 2014.

[12] J. D. Simeral *et al.*, "Home use of a percutaneous wireless intracortical brain-computer interface by individuals with tetraplegia," *IEEE Trans. Biomed. Eng.*, vol. 68, no. 7, pp. 2313–2325, Jul. 2021.

[13] M. Song *et al.*, "A 1.66 Gb/s and 5.8 pJ/b transcutaneous IR-UWB telemetry system with hybrid impulse modulation for intracortical brain-computer interfaces," in *IEEE Int. Solid-State Circuits Conf. (ISSCC) Dig. Tech. Papers*, Feb. 2022, pp. 394–396.

[14] M. Yin, D. A. Borton, J. Aceros, W. R. Patterson, and A. V. Nurmikko, "A 100-channel hermetically sealed implantable device for chronic wireless neurosensing applications," *IEEE Trans. Biomed. Circuits Syst.*, vol. 7, no. 2, pp. 115–128, Apr. 2013.

[15] C. Angelique Paulk *et al.*, "Large-scale neural recordings with single-cell resolution in human cortex using high-density Neuropixels probes," *Nature Neurosci.*, vol. 25, pp. 1–53, Jan. 2022.

[16] S. A. Mirbozorgi, H. Bahrami, M. Sawan, L. A. Rusch, and B. Gosselin, "A single-chip full-duplex high speed transceiver for multi-site stimulating and recording neural implants," *IEEE Trans. Biomed. Circuits Syst.*, vol. 10, no. 3, pp. 643–653, Jun. 2016.

[17] M. Li *et al.*, "Comparable investigation of characteristics for implant intra-body communication based on galvanic and capacitive coupling," *IEEE Trans. Biomed. Circuits Syst.*, vol. 13, no. 6, pp. 1747–1758, Dec. 2019.

[18] H. Kassiri *et al.*, "Rail-to-rail-Input dual-radio 64-channel closed-loop neurostimulator," *IEEE J. Solid-State Circuits*, vol. 52, no. 11, pp. 2793–2810, Nov. 2017.

[19] G. Breed *et al.*, "Basic principles of electrically small antennas," *High Freq. Electron.*, vol. 6, 2, pp. 50–53, 2007.

[20] S. Perez-Simbor, C. Andreu, C. Garcia-Pardo, M. Frasson, and N. Cardona, "UWB path loss models for ingestible devices," *IEEE Trans. Antennas Propag.*, vol. 67, no. 8, pp. 5025–5034, Aug. 2019.

[21] J. S. McLean, "A re-examination of the fundamental limits on the radiation Q of electrically small antennas," *IEEE Trans. Antennas Propag.*, vol. 44, no. 5, p. 672, May 1996.

[22] M. L. Wang, S. Baltsavias, T. C. Chang, M. J. Weber, J. Charthad, and A. Arbabian, "Wireless data links for next-generation networked micro-implantables," in *Proc. IEEE Custom Integr. Circuits Conf. (CICC)*, Apr. 2018, pp. 1–9.

[23] W. Li, Y. Duan, and J. Rabaey, "A 200-Mb/s energy efficient transcranial transmitter using inductive coupling," *IEEE Trans. Biomed. Circuits Syst.*, vol. 13, no. 2, pp. 435–443, Apr. 2019.

[24] P. Yeon, S. A. Mirbozorgi, J. Lim, and M. Ghovanloo, "Feasibility study on active back telemetry and power transmission through an inductive link for millimeter-sized biomedical implants," *IEEE Trans. Biomed. Circuits Syst.*, vol. 11, no. 6, pp. 1366–1376, Dec. 2017.

[25] T.-C. Yu, W.-H. Huang, and C.-L. Yang, "Design of dual frequency mixed coupling coils of wireless power and data transfer to enhance lateral and angular misalignment tolerance," *IEEE J. Electromagn., RF Microw. Med. Biol.*, vol. 3, no. 3, pp. 216–223, Sep. 2019.

[26] S. Mukherjee *et al.*, "25.4 A 500 Mb/s 200pJ/b die-to-die bidirectional link with 24kV surge isolation and 50kV/μs CMR using resonant inductive coupling in 0.18 μm CMOS," in *IEEE Int. Solid-State Circuits Conf. (ISSCC) Dig. Tech. Papers*, Feb. 2017, pp. 434–435.

[27] J. O. Mur-Miranda *et al.*, "Wireless power transfer using weakly coupled magnetostatic resonators," in *Proc. IEEE Energy Convers. Congr. Expo.*, Sep. 2010, pp. 4179–4186.

[28] A. De Marcellis, G. Di Patrizio Stanchieri, M. Faccio, E. Palange, and T. G. Constandinou, "A 300 Mbps 37 pJ/bit pulsed optical biotelemetry," *IEEE Trans. Biomed. Circuits Syst.*, vol. 14, no. 3, pp. 441–451, Jun. 2020.

[29] J. Bae and H.-J. Yoo, "The effects of electrode configuration on body channel communication based on analysis of vertical and horizontal electric dipoles," *IEEE Trans. Microw. Theory Techn.*, vol. 63, no. 4, pp. 1409–1420, Apr. 2015.

[30] M. A. Callejon, L. Fernandez-Jimenez, J. Reina-Tosina, and L. M. Roa, "Galvanic intrabody communication for brain stimulation: A finite-element simulation study," in *IEEE MTT-S Int. Microw. Symp. Dig.*, Seville, Spain, May 2017, pp. 19–21.

[31] M. Amparo Callejon, J. Reina-Tosina, D. Naranjo-Hernandez, and L. M. Roa, "Galvanic coupling transmission in intrabody communication: A finite element approach," *IEEE Trans. Biomed. Eng.*, vol. 61, no. 3, pp. 775–783, Mar. 2014.

[32] P. Chen, H. Yang, R. Luo, and B. Zhao, "All-digital galvanically-coupled BCC receiver resilient to frequency misalignment," *IEEE Trans. Biomed. Circuits Syst.*, vol. 11, no. 3, pp. 714–726, Jun. 2017.

[33] J.-H. Lee, K. Kim, M. Choi, J.-Y. Sim, H.-J. Park, and B. Kim, "A 16.6-pJ/b 150-Mb/s body channel communication transceiver with decision feedback equalization improving >200% area efficiency," in *Proc. Symp. VLSI Circuits*, Jun. 2017, pp. C62–C63.

[34] Y. He *et al.*, "A 28.2 μC neuromorphic sensing system featuring SNN-based near-sensor computation and event-driven body-channel communication for insertable cardiac monitoring," in *Proc. IEEE Asian Solid-State Circuits Conf. (A-SSCC)*, Nov. 2021, pp. 1–3.

[35] L. Bereuter *et al.*, "Fundamental characterization of conductive intracardiac communication for leadless multisite pacemaker systems," *IEEE Trans. Biomed. Circuits Syst.*, vol. 13, no. 1, pp. 237–247, Feb. 2018.

[36] A. Khaleghi, R. Noormohammadi, and I. Balasingham, "Conductive impulse for wireless communication in dual-chamber leadless pacemakers," *IEEE Trans. Microw. Theory Techn.*, vol. 69, no. 1, pp. 443–451, Jan. 2021.

[37] K. H. Lee, P. S. Duffy, and A. J. Bieber, *Deep Brain Stimulation: Indications and Applications*. Redwood City, CA, USA: Pan Stanford Publishing, 2016.

Authorized licensed use limited to: IMEC. Downloaded on September 15,2022 at 08:09:51 UTC from IEEE Xplore. Restrictions apply.

This article has been accepted for inclusion in a future issue of this journal. Content is final as presented, with the exception of pagination.

[38] J. Lim *et al.*, "A light-tolerant wireless neural recording IC for motor prediction with near-infrared-based power and data telemetry," *IEEE J. Solid-State Circuits*, vol. 57, no. 4, pp. 1061–1074, Apr. 2022.
[39] X. Yi, W. Zheng, H. Cao, S. Wang, X. Feng, and Z. Yang, "Wireless power transmission for implantable medical devices using focused ultrasound and a miniaturized 1–3 piezoelectric composite receiving transducer," *IEEE Trans. Ultrason., Ferroelectr., Freq. Control*, vol. 68, no. 12, pp. 3592–3598, Dec. 2021.
[40] Z. Kashani, S. J. Ilham, and M. Kiani, "Design and optimization of ultrasonic links with phased arrays for wireless power transmission to biomedical implants," *IEEE Trans. Biomed. Circuits Syst.*, vol. 16, no. 1, pp. 64–78, Feb. 2022.
[41] S. Gabriel, R. W. Lau, and C. Gabriel, "The dielectric properties of biological tissues: III. Parametric models for the dielectric spectrum of tissues," *Phys. Med. Biol.*, vol. 41, no. 11, pp. 2271–2293, Nov. 1996.
[42] P. A. Hasgall *et al.*, "IT'IS database for thermal and electromagnetic parameters of biological tissues," IT'IS Found., Zürich, Switzerland, Tech. Rep. Version 4.1, Feb. 2022.
[43] F. B. Haeussinger, S. Heinzel, T. Hahn, M. Schecklmann, A.-C. Ehlis, and A. J. Fallgatter, "Simulation of near-infrared light absorption considering individual head and prefrontal cortex anatomy: Implications for optical neuroimaging," *PLoS ONE*, vol. 6, no. 10, Oct. 2011, Art. no. e26377.
[44] *AC/DC Module User's Guide*, Comsol Multiphys., Burlington, VT, USA, 2015.
[45] T. Nunen *et al.*, "DIY electromagnetic phantoms for biomedical wireless power transfer experiments," in *Proc. IEEE Wireless Power Transf. Conf.*, Jun. 2019, pp. 399–404.
[46] M. A. Callejon, J. Reina-Tosina, D. Naranjo-Hernandez, and L. M. Roa, "Measurement issues in galvanic intrabody communication: Influence of experimental setup," *IEEE Trans. Biomed. Eng.*, vol. 62, no. 11, pp. 2724–2732, Nov. 2015.
[47] B. Kibret, M. Seyedi, D. T. H. Lai, and M. Faulkner, "Investigation of galvanic-coupled intrabody communication using the human body circuit model," *IEEE J. Biomed. Health Informat.*, vol. 18, no. 4, pp. 1196–1206, Jul. 2014.
[48] Y. Feng, T. M. Abney, R. J. Okamoto, R. B. Pless, G. M. Genin, and P. V. Bayly, "Relative brain displacement and deformation during constrained mild frontal head impact," *J. Roy. Soc. Interface*, vol. 7, no. 53, pp. 1677–1688, Dec. 2010.
[49] J.-Y. Son and H.-K. Cha, "An implantable neural stimulator IC with anodic current pulse modulation based active charge balancing," *IEEE Access*, vol. 8, pp. 136449–136458, 2020.
[50] B. Chatterjee *et al.*, "A 1.15 μW 5.54 mm^3 implant with a bidirectional neural sensor and stimulator SoC utilizing bi-phasic quasi-static brain communication achieving 6kbps-10 Mbps uplink with compressive sensing and RO-PUF based collision avoidance," in *Proc. VLSI Circuits*, Jun. 2021, pp. 1–2.

Chengyao Shi (Student Member, IEEE) received the B.S. and M.S. degrees from the University of Padua, Padua, Italy, in 2017 and 2020, respectively. He is currently pursuing the Ph.D. degree at the Eindhoven University of Technology (TU/e), Eindhoven, The Netherlands.

He is currently with imec, Eindhoven. His current research interests include body area network and intrabody communication.

Minyoung Song (Member, IEEE) received the B.S. and Ph.D. degrees in electrical engineering from Korea University, Seoul, South Korea, in 2006 and 2013, respectively.

He was a Senior Engineer with Samsung Electronics, Hwaseong, South Korea, from 2013 to 2016. He was a Visiting Scholar with the University of California, Los Angeles, Los Angeles, CA, USA, from 2008 to 2009. He joined the University of California Santa Cruz, Santa Cruz, CA, USA, as a Visiting Scholar, in 2012. He has been with the imec, Eindhoven, The Netherlands, since 2016, where he is currently a Senior Researcher. His current research interests are energy-efficient digitally assisted RFIC, frequency synthesizers/clock generators, and high-speed wireline transceivers.

Dr. Song was a recipient of the IEEE Seoul Section Student Paper Contest Bronze Award in 2007 and 2010, respectively.

Zhenyu Gao received the Ph.D. degree from the Erasmus University Medical Center, Rotterdam, The Netherlands, in 2011.

He was a Post-Doctoral Researcher with the Netherland Institute for Neuroscience, Amsterdam, The Netherlands, and later as an Assistant Professor with the Department Neuroscience, Erasmus University Medical Center, from 2012 to 2017. He is currently an Associate Professor with the Department Neuroscience, Erasmus University Medical Center. His current research interests focus on dissecting functional brain circuits and understanding their specific roles in healthy and diseased brains.

Dr. Gao was a recipient of the NWO VIDI Grant and European Research Council (ERC) Starting Grant.

Andrea Bevilacqua (Senior Member, IEEE) received the Laurea and Ph.D. degrees in electronics engineering from the University of Padua, Padua, Italy, in 2000, and 2004, respectively.

From 2005 to 2015, he was an Assistant Professor with the Department of Information Engineering, University of Padova, where he is currently an Associate Professor. He has authored or coauthored of more than 100 technical articles, and he holds six patents. His current research interests include the design of analog and RF/microwave integrated circuits and the analysis of wireless communication systems, radars, and dc–dc converters.

Dr. Bevilacqua was an ITPC Member of the IEEE ISSCC from 2017 to 2021. He served on the TPC for the IEEE ESSCIRC from 2007 to 2019. He was the TPC Co-Chair of the IEEE ESSCIRC 2014. He was a TPC Member of the IEEE ICUWB from 2008 to 2010. He was an Associate Editor of the IEEE TRANSACTIONS OF CIRCUITS AND SYSTEMS II from 2011 to 2013 and was nominated as the Best Associate Editor for the IEEE TRANSACTIONS OF CIRCUITS AND SYSTEMS II from 2012 to 2013. He served as a Guest Editor for the Special Issue of the IEEE JOURNAL OF SOLID-STATE CIRCUITS dedicated to ESSCIRC 2017. He served in the Distinguished Lecturer Program for the IEEE Solid-State Circuits Society during 2020–2021.

Guido Dolmans received the M.Sc. and Ph.D. degrees in electrical engineering from the Eindhoven University of Technology (TU/e), Eindhoven, The Netherlands, in 1992 and 1997, respectively.

He was a Senior Scientist with Philips Research, Eindhoven, from 1997 to 2006. In 2014, he returned to TU/e as a Full Professor, while continuing to work at imec, Eindhoven. He has been the Scientific Director and Research and Development Manager with imec, since 2006. He has coauthored over 100 articles in scientific/technical journals and proceedings and holds 14 U.S. patents. His primary research interests are circuits and systems for wireless communications, localization, radar, artificial intelligence (AI), and data science.

Yao-Hong Liu (Senior Member, IEEE) received the Ph.D. degree from National Taiwan University, Taipei, Taiwan, in 2009.

He was with Intel, Xindien, Taiwan, and Mobile Devices, Taipei, from 2002 to 2010, where he is developing wireless transceiver ICs. Since 2010, he has been with imec, Eindhoven, The Netherlands, where he is leading the research of the ultralow power ASIC design. He is currently the Scientific Director of imec and a Distinguished Research Associate with Technical University Eindhoven, Eindhoven. His current research focuses on wireless technologies for implantable brain–computer interfaces and Internet of Things (IoT).

Dr. Liu served as a Technical Program Committee Member for the IEEE ISSCC and is currently a Steering Committee Member of the IEEE RFIC Symposium. He was a recipient of the European Research Council (ERC) Consolidator Grant.

Authorized licensed use limited to: IMEC. Downloaded on September 15,2022 at 08:09:51 UTC from IEEE Xplore. Restrictions apply.